


Reduced nuclear helicity amplitudes for deuteron electrodisintegration and other processes

J. Flores  and S. S. Chabysheva

Department of Physics, University of Idaho, Moscow, Idaho 83844, USA

J. R. Hiller 

Department of Physics, University of Idaho, Moscow, Idaho 83844, USA

and Department of Physics and Astronomy, University of Minnesota-Duluth, Duluth, Minnesota 55812, USA



(Received 5 January 2023; accepted 4 April 2023; published 20 April 2023)

We extend the original idea of reduced nuclear amplitudes to capture individual helicity amplitudes and discuss various applications to exclusive processes involving the deuteron. Specifically, we consider deuteron form factors, structure functions, tensor polarization observables, photodisintegration, and electrodisintegration. The basic premise is that nuclear processes at high momentum transfer can be approximated by tree graphs for point-like nucleons supplemented by empirical form factors for each nucleon. The latter represent the internal structure of the nucleon, and incorporate nonperturbative physics, which can allow for early onset of scaling behavior. The nucleon form factors are evaluated at the net momentum transfer experienced by the given nucleon, with use of G_E for a no-flip contribution and G_M for a helicity-flip contribution. Results are compared with data where available. The deuteron photodisintegration asymmetry Σ is obtained with a value of $\Sigma(90^\circ) \simeq -0.06$, which is much closer to experiment than the value of -1 originally expected. The method also provides an estimate of the momentum transfer values required for scaling onset. We find that the deuteron structure function B is a good place to look, above momentum transfers of 10 GeV^2 .

DOI: [10.1103/PhysRevC.107.045205](https://doi.org/10.1103/PhysRevC.107.045205)

I. INTRODUCTION

With the advent of the upgraded electron accelerator at the Thomas Jefferson National Accelerator Facility, scattering experiments with polarized beams and targets at high energy and high momentum transfer become possible. In the regime of high momentum transfer to all relevant nucleons, quantum chromodynamics (QCD) implies that the internal structure of every nucleon is important. Until *ab initio* QCD (lattice) calculations for nuclear scattering processes are available for more than very simple processes, one is led to consider models that can represent the basic physics.

One such approach is the reduced nuclear amplitude (RNA) analysis pioneered by Brodsky and Chertok [1]. In addition to their application to a generic deuteron form factor, the approach has been applied to deuteron disintegration [2], pion photoproduction [3], and photodisintegration of ^3He [4]. As originally developed, a nuclear process was modeled as a tree-level amplitude multiplied by a generic form factor for each nucleon, with each form factor evaluated at the net momentum transferred to that nucleon. In order to model the behavior of polarization observables [5–15], we extend this approach to a reduced nuclear helicity amplitude (RNHA) method to combine a tree-level helicity amplitude for point-like nucleons with the appropriate form factor for each nucleon. When the nucleon does (not) flip its helicity, we use the electric (magnetic) form factor G_{EN} (G_{MN}). As a check on the procedure, virtual photon absorption by a single nucleon in the RNHA approach is consistent with the definitions of G_{EN} and G_{MN} .

A caveat in applications of the RNA approach is that the normalization is not determined by the model and is fixed to data at infinite momentum transfer by the coefficient of the leading power-law behavior. This means that the normalization cannot be determined in practice; fitting to a data point at some intermediate kinematics will give the wrong normalization and the wrong magnitude at higher momentum transfer. Instead, ratios need to be considered, so that the normalization becomes irrelevant.

The primary criterion for the asymptotic region is in the momentum transfer to each nucleon. For every nucleon in the process, the momentum transfer must be above some common threshold, which is at least 1 GeV^2 . For example, for deuteron photodisintegration, the momentum transfer to a nucleon is $-t_N = -(p_N - p/2)^2$, where p_N is the final four-momentum of the nucleon and p is the initial deuteron momentum. When expressed in terms of the photon energy E_γ and the final nucleon angle θ , the constraint to be above 1 GeV^2 becomes [16]

$$m_N E_\gamma \left[1 - \sqrt{\frac{E_\gamma}{m_N + E_\gamma}} |\cos \theta| \right] \geq 1 \text{ GeV}^2. \quad (1.1)$$

This relationship is illustrated in Fig. 1. Notice that away from 90° , the lower limit is quite high. For electrodisintegration, only the most recent data [17, 18] begins to reach this threshold.

Here, we will focus on deuteron processes, including photodisintegration and electrodisintegration. For recent reviews of deuteron studies at high momentum transfer, see

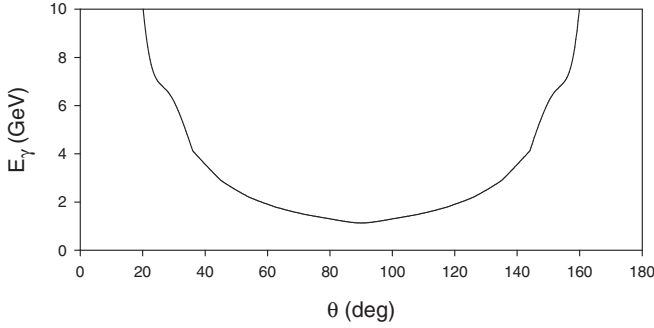


FIG. 1. Angular dependence of the scale for large momentum transfer in deuteron photodisintegration.

[16,19,20]. Elastic electron scattering data at high momentum transfer is presented in [21–25]. Recent photodisintegration data can be found in [26–29], and for electrodisintegration data, in [17,18,30–33]. Other analyses of deuteron processes include hidden-color contributions to deuteron form factors [34], the hard rescattering mechanism [35], quark-gluon strings [36], the Moscow NN potential [37], and anti-de Sitter (AdS)/QCD models [38,39].

One recent experiment [17] used the 10.6 GeV electron beam at JLab and the Hall C spectrometers to measure electron scattering from a liquid deuterium target. The final electron and the proton were detected, with the kinematics restricted to the exclusive process $ed \rightarrow e'pn$. One spectrometer measured the final electron at a nominal 12.2° degrees from the beam direction, with a momentum of 8.5–9.1 GeV such that the recorded events had a distribution of momentum transfer squared reaching 5 GeV^2 . The events studied were taken from a bin of $4.5 \pm 0.5 \text{ GeV}^2$ in the tail of the distribution; however, the nominal transfer was 4.2 GeV^2 , because the majority of the events were in the lower half of the bin.

A second spectrometer measured the proton momentum at a range of angles to the beam direction, tuned to select events where the (missing) neutron had an angle relative to the direction of the momentum transfer that fell within a chosen bin. In the one-photon exchange approximation, which we assume, the momentum transferred is, of course, the photon momentum. The published neutron angles are binned at 35° , 45° , and 75° , with the first two selected to minimize final-state interactions. For our purposes, the importance of these two angles is that the momentum transferred to the neutron reaches 1 GeV in a zero-binding approximation, so that, rather than focus on the internal structure of the deuteron, we can consider the response to a large momentum transfer to all the nucleons involved and we can see that experiments may be approaching the threshold where our model can be applied.

The RNHA model is constructed in detail in Sec. II for two-nucleon processes. In the remainder of the paper, we consider various processes for the deuteron. In Sec. III, the form factors,¹ structure functions, and tensor polarization observables of elastic electron scattering from the deuteron are obtained. Photodisintegration and electrodisintegration are analyzed in

Secs. IV and V. Within the zero-binding approximation, elastic scattering and photodisintegration live at edges of the kinematic range of electrodisintegration and are essentially special cases that provide introductory examples. Section VI contains a summary of the results and suggestions for additional applications. Many details of the electrodisintegration helicity amplitudes are left to an Appendix.

II. CONSTRUCTION OF THE MODEL

The basic process for a two-nucleon system to absorb a photon and exchange momentum between the nucleons is illustrated in Fig. 2. These diagrams are modeled on the primitive process of $\gamma^* ff \rightarrow ff$, with f representing a point-like nucleon.² The structure of each nucleon is then introduced by combining the Feynman amplitude for each diagram with the appropriate form factor for each nucleon, evaluated at the net momentum transfer for that nucleon. For a deuteron process in the zero-binding limit, the initial nucleons share the initial deuteron momentum p equally, so that $p_p = p_n = p/2$. We also neglect the nucleon mass difference, setting $m_p = m_n \equiv m$. The distinction between different photon-absorption processes is then in the nature of the photon, being either real or virtual, and in the outcome for the final nucleons, bound as a deuteron or not.

The tree-level amplitudes for the four diagrams in Fig. 2 are

$$M_a^v(\lambda'_p, \lambda'_n, \lambda_p, \lambda_n) = A_p^{\mu\nu}(p/2 + q; \lambda'_p, \lambda_p) \frac{1}{(p'_n - p/2)^2} B_{n\mu}(\lambda'_n, \lambda_n), \quad (2.1)$$

$$M_b^v(\lambda'_p, \lambda'_n, \lambda_p, \lambda_n) = A_p^{\mu\nu}(p'_p - q; \lambda'_p, \lambda_p) \frac{1}{(p'_n - p/2)^2} B_{n\mu}(\lambda'_n, \lambda_n), \quad (2.2)$$

$$M_c^v(\lambda'_p, \lambda'_n, \lambda_p, \lambda_n) = A_n^{\mu\nu}(p/2 + q; \lambda'_n, \lambda_n) \frac{1}{(p'_p - p/2)^2} B_{p\mu}(\lambda'_p, \lambda_p), \quad (2.3)$$

$$M_d^v(\lambda'_p, \lambda'_n, \lambda_p, \lambda_n) = A_n^{\mu\nu}(p'_n - q; \lambda'_n, \lambda_n) \frac{1}{(p'_p - p/2)^2} B_{p\mu}(\lambda'_p, \lambda_p), \quad (2.4)$$

where

$$A_N^{\mu\nu}(p; \lambda'_N, \lambda_N) = \bar{u}'_N \gamma^\mu \frac{\not{p} + m}{p^2 - m^2} \gamma^\nu u_N, \\ B_N^\mu(\lambda'_N, \lambda_N) = \bar{u}'_N \gamma^\mu u_N \quad (2.5)$$

with u_N (\bar{u}'_N) the initial (final) spinor for the nucleon N with helicity λ_N (λ'_N). The subamplitude A_N represents the

²In [2], the primitive process was $\gamma^* q\bar{q} \rightarrow q\bar{q}$, with q corresponding to a point-like proton and \bar{q} to a point-like neutron, and direct interaction of the photon with the neutron was neglected. Here, we amend and extend this, to retain information about helicity states of the fermions and include photon absorption by the neutron.

¹For discussion specifically in terms of perturbative QCD, see [34].

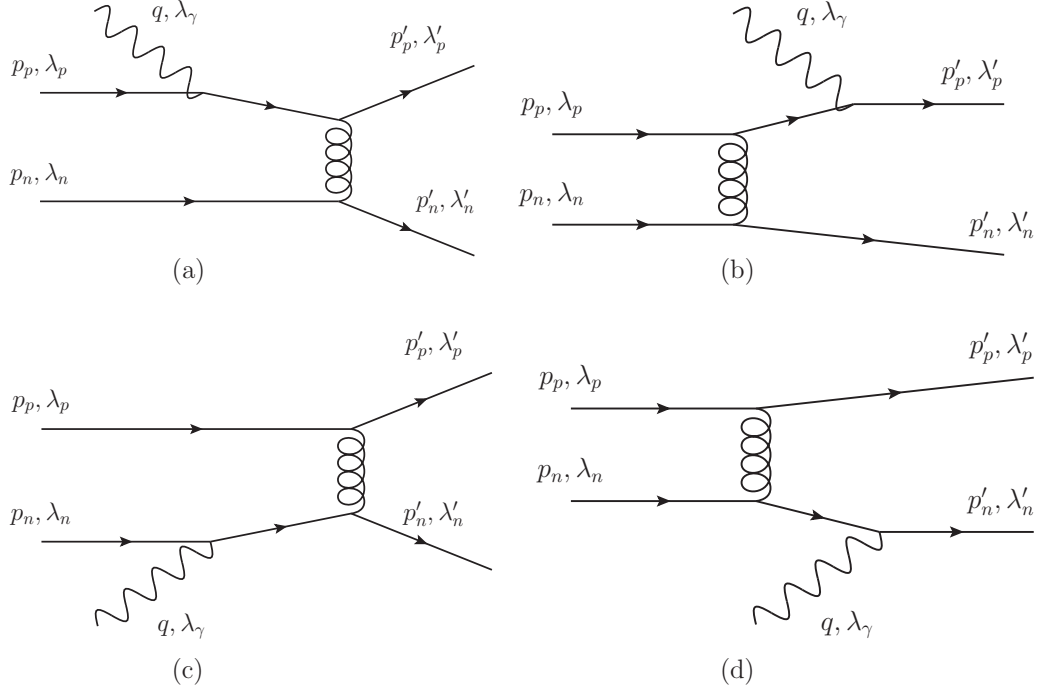


FIG. 2. Tree graphs for deuteron processes that absorb a photon of momentum q and helicity λ_γ . The initial (final) nucleon momentum and helicity are p_N (p'_N) and λ_N (λ'_N), with $N = p$ or n . The two nucleons exchange momentum via a vector particle. The four diagrams differ in the nature of the photon-absorbing nucleon and the order of this absorption and momentum transfer between nucleons.

fermion line that absorbs the photon, and B_N represents the other fermion line. Calculation of these subamplitudes can be checked against the trace theorem for sums over helicities:

$$\sum_{\lambda_N, \lambda'_N} A_N^{\nu\mu'*}(p; \lambda'_N, \lambda_N) A_N^{\mu\nu}(p; \lambda'_N, \lambda_N) = \text{Tr} \left[\gamma^\nu \frac{\not{p} + m}{p^2 - m^2} \gamma^{\mu'} (\not{p}'_N + m) \gamma^\mu \frac{\not{p} + m}{p^2 - m^2} \gamma^\nu (\not{p}'_N + m) \right], \quad (2.6)$$

$$\sum_{\lambda_N, \lambda'_N} B_N^{\mu'*}(\lambda'_N, \lambda_N) B_N^\mu(\lambda'_N, \lambda_N) = \text{Tr} [\gamma^{\mu'} (\not{p}'_N + m) \gamma^\mu (\not{p}'_N + m)]. \quad (2.7)$$

The full amplitude is constructed from the M_X by combining them with form factors for each nucleon. For a deuteron with initial helicity λ_d , we have

$$M^\nu(\lambda'_p, \lambda'_n, \lambda_d) = \sum_{\lambda_p, \lambda_n} C_{\lambda_p \lambda_n}^{\lambda_d} \left[\sum_{X=a,b,c,d} M_X^\nu(\lambda'_p, \lambda'_n, \lambda_p, \lambda_n) \right] \times G_{p\lambda'_p \lambda_p}(Q_p^2) G_{n\lambda'_n \lambda_n}(Q_n^2), \quad (2.8)$$

where $Q_N^2 = -(p'_N - p_N)^2$,

$$C_{\lambda_p \lambda_n}^{\lambda_d} = \begin{cases} \delta_{\lambda_p \pm \frac{1}{2}} \delta_{\lambda_n \pm \frac{1}{2}}, & \lambda_d = \pm 1, \\ \frac{1}{\sqrt{2}} (\delta_{\lambda_p \frac{1}{2}} \delta_{\lambda_n - \frac{1}{2}} + \delta_{\lambda_p - \frac{1}{2}} \delta_{\lambda_n + \frac{1}{2}}), & \lambda_d = 0, \end{cases} \quad (2.9)$$

and

$$G_{N\lambda'\lambda} = \begin{cases} G_{EN}, & \lambda' = \lambda, \\ G_{MN}, & \lambda' = -\lambda. \end{cases} \quad (2.10)$$

The form factors G_{EN} and G_{MN} represent the internal structure of the nucleons. They can be represented by data or empirical fits. For simplicity, we use the fits [40]

$$G_{Ep} \simeq \left(1 + \frac{Q_N^2}{m_0^2} \right)^{-2}, \quad G_{Mp} \simeq \mu_p G_{Ep}, \\ G_{Mn} \simeq \mu_n G_{Ep}, \quad G_{En} \simeq -\frac{\mu_n \tau}{1 + 5.6\tau} G_{Ep}, \quad (2.11)$$

where $m_0^2 = 0.71 \text{ GeV}^2$, $\tau = \frac{Q_N^2}{4m^2}$, $\mu_p = 2.79$, and $\mu_n = -1.91$. To limit the analysis to a single mass scale, we take the parameter m_0 to be proportional to the nuclear mass, with $m_0^2 = 0.80 m^2$. We do not attempt to compute or assign an overall normalization to M^ν , and the running of the strong coupling constant is not included.

The initial nucleon spinor, for a deuteron traveling along the negative z direction, is [41]

$$u_N = \frac{\not{p}/2 + m}{\sqrt{E_d/2 + m}} \begin{pmatrix} \phi^{(\lambda_N)}(-\hat{z}) \\ 0 \end{pmatrix} \quad (2.12)$$

with

$$\phi^{(1/2)}(-\hat{z}) = \begin{pmatrix} 0 \\ 1 \end{pmatrix}, \quad \phi^{(-1/2)}(-\hat{z}) = \begin{pmatrix} 1 \\ 0 \end{pmatrix}. \quad (2.13)$$

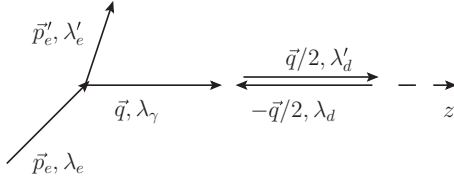


FIG. 3. Kinematics for elastic electron-deuteron scattering in the Breit frame. The photon travels along the positive z direction, and the deuteron comes from the right, along the negative z direction.

The final nucleon spinor is

$$u'_N = \frac{\not{p}'_N + m}{\sqrt{E'_N + m}} \begin{pmatrix} \phi^{(\lambda'_N)}(\hat{p}'_N) \\ 0 \end{pmatrix} \quad (2.14)$$

with

$$\begin{aligned} \phi^{(1/2)}(\hat{p}'_N) &= \begin{pmatrix} \cos(\theta_N/2) \\ e^{i\phi_N} \sin(\theta_N/2) \end{pmatrix}, \\ \phi^{(-1/2)}(\hat{p}'_N) &= \begin{pmatrix} -e^{-i\phi_N} \sin(\theta_N/2) \\ \cos(\theta_N/2) \end{pmatrix}, \end{aligned} \quad (2.15)$$

where θ_N and ϕ_N are the polar and azimuthal angles of the outgoing momentum of the particular nucleon.

As discussed in the Introduction, the overall normalization of the RNHA amplitude is unknown. For comparison with data, we consider quantities which are themselves ratios or a ratio of the model to data.

III. ELASTIC ELECTRON SCATTERING

A. Form factors

The three deuteron form factors, G_C , G_M , and G_Q , are readily obtained from the hadronic helicity amplitudes of elastic electron-deuteron scattering in the Breit frame [42]. The kinematics are shown in Fig. 3. The photon four-momentum is $q = (0, 0, 0, q_z)$ and the initial (final) deuteron four-momentum is $p = (E_d, 0, 0, -q_z/2)$ ($p' = (E_d, 0, 0, q_z/2)$), with $q_z^2 = Q^2$ and $E_d = \sqrt{Q^2/4 + m_d^2}$. In the zero-binding limit,³ $m_d = 2m$ and the individual nucleon four-momenta are $p_p = p_n = p/2$ and $p'_p = p'_n = p'/2$. The hadronic matrix elements are given by

$$G_{\lambda'_d, \lambda_d}^\mu = \sum_{\lambda'_p, \lambda'_n} C_{\lambda'_p \lambda'_n}^{\lambda'_d} M^\mu(\lambda'_p, \lambda'_n, \lambda_d). \quad (3.1)$$

The initial spinors are as in Eq. (2.12); the final spinors are specified by

$$u'_N = \frac{\not{p}'/2 + m}{\sqrt{E_d/2 + m}} \begin{pmatrix} \phi^{(\lambda'_N)}(\hat{z}) \\ 0 \end{pmatrix}. \quad (3.2)$$

³The difference between the proton and neutron masses is neglected in addition to the deuteron binding energy, the two being of the same order.

The three form factors are then extracted as [42,43]

$$\begin{aligned} G_C &= \frac{-1}{2m_d \sqrt{1+\eta}} \frac{G_{00}^+ - 2G_{+-}^+}{3}, \quad G_M = \frac{2}{2m_d \sqrt{1+\eta}} \frac{G_{+0}^x}{\sqrt{2\eta}}, \\ G_Q &= \frac{-1}{2m_d \sqrt{1+\eta}} \frac{G_{00}^+ + G_{+-}^+}{2\eta} \end{aligned} \quad (3.3)$$

with $\eta \equiv \frac{Q^2}{4m_d^2}$ and the $+$ superscript denoting the light-front sum of the 0 and z components. For the helicity matrix elements, the model yields the following Q^2 dependence:

$$G_{00}^+ = 0.5588 \mathcal{N} m \left(\frac{m}{Q}\right)^9 \left[1 + 129.1 \frac{m^2}{Q^2} + \mathcal{O}\left(\frac{m^4}{Q^4}\right) \right], \quad (3.4)$$

$$G_{+-}^+ = -69.85 \mathcal{N} m \left(\frac{m}{Q}\right)^{11} \left[1 + 4.8 \frac{m^2}{Q^2} + \mathcal{O}\left(\frac{m^4}{Q^4}\right) \right], \quad (3.5)$$

$$G_{+0}^x = 8.851 \mathcal{N} m \left(\frac{m}{Q}\right)^{10} \left[1 + 4.8 \frac{m^2}{Q^2} + \mathcal{O}\left(\frac{m^4}{Q^4}\right) \right] \quad (3.6)$$

with \mathcal{N} the unknown normalization. The factor of m/Q associated with each helicity flip [44] is clearly evident. For the form factors, we find

$$G_C = -\frac{0.5588}{\sqrt{1+\eta}} \frac{\mathcal{N}}{12} \left(\frac{m}{Q}\right)^9 \left[1 + 379.1 \frac{m^2}{Q^2} + \mathcal{O}\left(\frac{m^4}{Q^4}\right) \right], \quad (3.7)$$

$$G_M = \frac{8.851}{\sqrt{\eta(1+\eta)}} \frac{\mathcal{N}}{2\sqrt{2}} \left(\frac{m}{Q}\right)^{10} \left[1 + 4.8 \frac{m^2}{Q^2} + \mathcal{O}\left(\frac{m^4}{Q^4}\right) \right], \quad (3.8)$$

$$G_Q = -\frac{0.5588}{\eta \sqrt{1+\eta}} \frac{\mathcal{N}}{8} \left(\frac{m}{Q}\right)^9 \left[1 + 4.086 \frac{m^2}{Q^2} + \mathcal{O}\left(\frac{m^4}{Q^4}\right) \right]. \quad (3.9)$$

The leading \pm signs are as expected for large Q^2 .

We have left the kinematic factor $\eta = Q^2/16m^2$ without substitution, because there can be three regimes for Q^2 . In addition to Q^2 large or small, there can be an intermediate region where Q^2 is large but η is not. Such an intermediate regime does exist for G_M and G_Q , where the coefficients of the nonleading terms are small enough for this correction to be small while η is also small. For G_C , this is not the case, because the coefficient of the nonleading term is large enough to require a Q^2 value for which η is also large. In the intermediate regime, we obtain

$$G_M \sim \left(\frac{m}{Q}\right)^{11}, \quad G_Q \sim \left(\frac{m}{Q}\right)^{11}, \quad (3.10)$$

and for the large- η regime

$$G_C \sim \left(\frac{m}{Q}\right)^{10}, \quad G_M \sim \left(\frac{m}{Q}\right)^{12}, \quad G_Q \sim \left(\frac{m}{Q}\right)^{12}. \quad (3.11)$$

Ratios of these form factors at very large Q^2 can be compared with the tree-level ratios for a point-like spin-one particle, such as the W^+ , which are [43]

$$\frac{G_C}{G_Q} = \frac{2}{3}\eta - 1, \quad \frac{G_M}{G_Q} = -2. \quad (3.12)$$

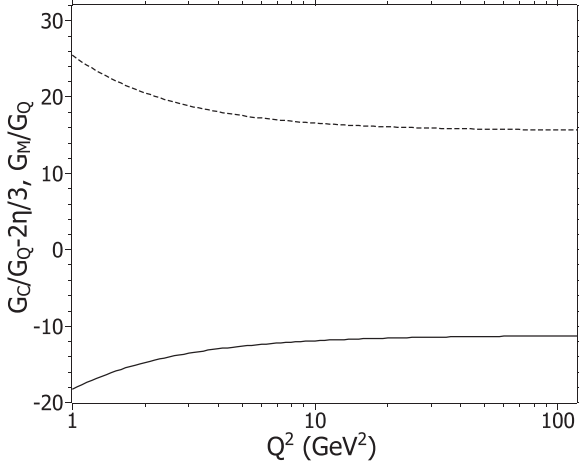


FIG. 4. Ratios $G_C/G_Q - 2\eta/3$ (dashed lines) and G_M/G_Q (solid lines) for the model deuteron form factors.

Such behavior is immediately reproduced for form factors separated according to a Drell-Yan frame [45], with the assumption of strict G_{00}^+ dominance [43]. In terms of our hadronic matrix elements, we have

$$\frac{G_C}{G_Q} = \frac{2}{3}\eta - 2\eta \frac{G_{+-}^+}{G_{00}^+ + G_{+-}^+}, \quad \frac{G_M}{G_Q} = -2\sqrt{2}\eta \frac{G_{+0}^x}{G_{00}^+ + G_{+-}^+}. \quad (3.13)$$

As already observed in [43], these Breit-frame ratios cannot both be resolved by simply assuming G_{00}^+ dominance. From our model, we obtain

$$\frac{G_C}{G_Q} = \frac{2}{3}\eta + 15.6 + \mathcal{O}\left(\frac{m^2}{Q^2}\right), \quad \frac{G_M}{G_Q} = -11.2 + \mathcal{O}\left(\frac{m^2}{Q^2}\right). \quad (3.14)$$

The leading $\frac{2}{3}\eta$ is just kinematic. The deviations of 15.6 and -11.2 from -1 and -2 , respectively, are due to nonleading contributions multiplied by powers of η . Similar deviations will arise for calculations done in the Drell-Yan frame, because η factors again interfere with strict G_{00}^+ dominance. Plots of these ratios are shown in Fig. 4.

B. Structure functions

Experiments designed to extract these form factors measure cross sections and polarization observables in elastic electron-deuteron scattering. The unpolarized cross section

$$\frac{d\sigma}{d\Omega} \propto S, \quad S \equiv A(Q^2) + B(Q^2) \tan^2(\theta_e/2) \quad (3.15)$$

depends on the electron scattering angle θ_e and two structure functions

$$A(Q^2) \equiv G_C^2 + \frac{8}{9}\eta^2 G_Q^2 + \frac{2}{3}\eta G_M^2, \quad (3.16)$$

$$B(Q^2) \equiv \frac{4}{3}\eta(1 + \eta)G_M^2. \quad (3.17)$$

These have been measured at the highest Q^2 yet attained at JLab [22–24], and A has been measured at comparable Q^2 at SLAC [21]. However, these do not yet reach the Q^2 values

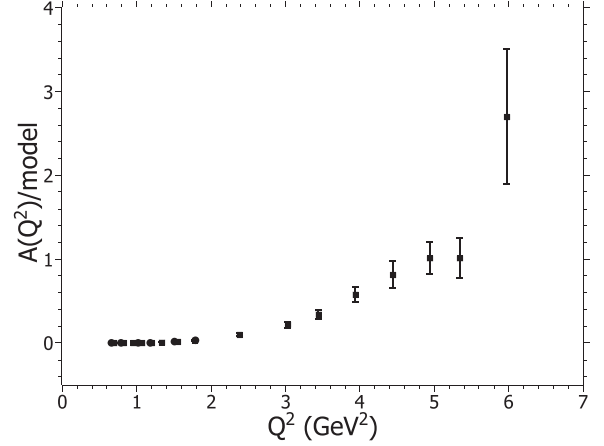


FIG. 5. Data for the deuteron structure function $A(Q^2)$ divided by the model function, including an arbitrary normalization. Experimental values are taken from [23] (circles) and [24] (squares).

needed for a definitive comparison. Figures 5 and 6 show plots of the data divided by the model, including an arbitrary normalization factor.

In our model, expansions of these functions in inverse powers of Q^2 are

$$A(Q^2) = 0.1041\mathcal{N}^2 \left(\frac{m}{Q}\right)^{20} \left[1 + 1246 \frac{m^2}{Q^2} + \mathcal{O}\left(\frac{m^4}{Q^4}\right) \right], \quad (3.18)$$

$$B(Q^2) = 13.06\mathcal{N}^2 \left(\frac{m}{Q}\right)^{20} \left[1 + 9.6 \frac{m^2}{Q^2} + \mathcal{O}\left(\frac{m^4}{Q^4}\right) \right]. \quad (3.19)$$

Because the expansion for G_C is valid only for large η , we have used the explicit form of η in constructing the expansion for A . The function B is independent of η ; the leading factor of $\eta(1 + \eta)$ in its definition exactly cancels against factors in the relationship of G_M to hadronic matrix elements. The expansion for B converges much faster than the expansion for A , and the leading Q^2 behavior is dominant for $Q^2 \gg 10 \text{ GeV}^2$ only for B . For A , one must wait until impossibly large Q^2 , which enters a regime where the collective quark

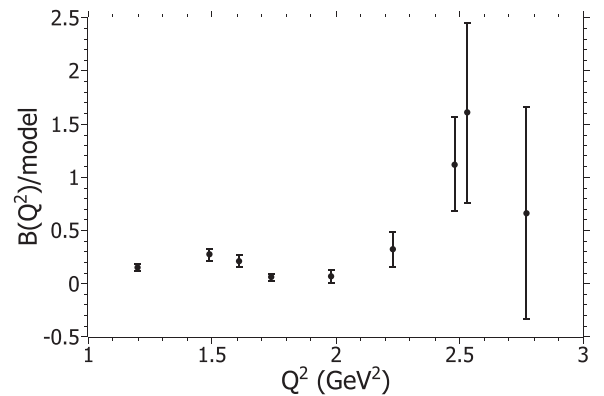
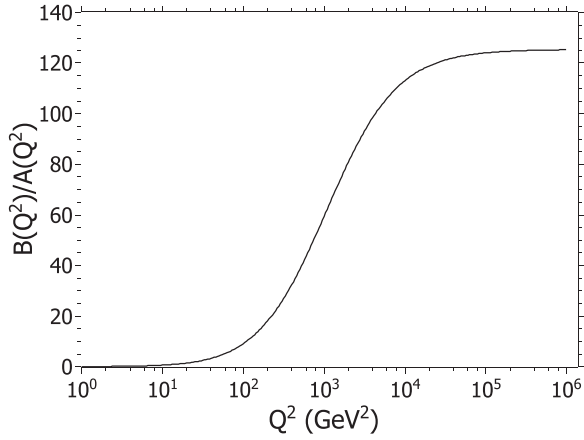


FIG. 6. Data for the deuteron structure function $B(Q^2)$ divided by the model function, including an arbitrary normalization. Experimental values are taken from [22].

FIG. 7. Ratio of B to A for the model deuteron structure functions.

substructure is important, including hidden-color effects [34], and the point-like approximation used in our model is invalid.

In [22] the large Q^2 behavior of B is quoted as being Q^{-24} from perturbative QCD. This faster fall off compared to A is attributed to the extra suppression of the helicity flip involved in G_M . However, there are other compensating factors, and, just as in our model, the behavior of B should be Q^{-20} , which is the same as A . In Fig. 7 we plot the ratio of B to A for a large range of Q^2 . This ratio becomes constant at very large Q^2 . Although the plots begin at low Q^2 , there is nothing in the model that could reproduce diffractive minima, hence the smooth appearance.

C. Tensor polarization observables

Experiments can also extract tensor polarization observables [20,25]

$$t_{20} \equiv -\frac{1}{\sqrt{2}S} \left[\frac{8}{3} \eta G_C G_Q + \frac{8}{9} \eta^2 G_Q^2 + \frac{1}{3} \eta (1 + 2(1 + \eta) \tan^2(\theta_e/2)) G_M^2 \right], \quad (3.20)$$

$$t_{21} \equiv \frac{2\eta}{\sqrt{3}S \cos(\theta_e/2)} \sqrt{\eta + \eta^2 \sin^2(\theta_e/2)} G_M G_Q, \quad (3.21)$$

$$t_{22} \equiv -\frac{\eta}{2\sqrt{3}S} G_M^2. \quad (3.22)$$

The highest Q^2 measurements of these were also done at JLab [25]. When η is held explicit, expansions in m/Q are

$$t_{20} = -\sqrt{2} + 1064[1 + 2(1 + \eta) \tan^2(\theta_e/2)] \left(\frac{m}{Q} \right)^2 + \mathcal{O}\left(\frac{m^4}{Q^4} \right), \quad (3.23)$$

$$t_{21} = 38.8 \sec(\theta_e/2) \sqrt{\eta + \sin^2(\theta_e/2)} \frac{m}{Q} + \sec(\theta_e/2) \sqrt{\eta + \sin^2(\theta_e/2)} [48606 + 77869(1 + \eta) \times \tan^2(\theta_e/2)] \left(\frac{m}{Q} \right)^3 + \mathcal{O}\left(\frac{m^4}{Q^4} \right), \quad (3.24)$$

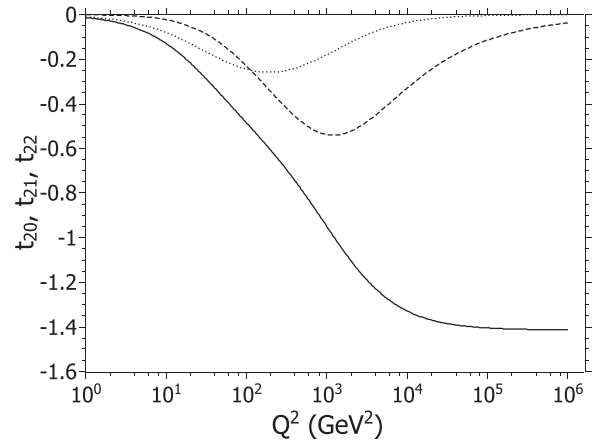


FIG. 8. Deuteron tensor polarization observables t_{20} (solid line), t_{21} (dashed line), and t_{22} (dotted line) as computed in the model at an angle of $\theta_e = 0^\circ$. The asymptotic value of $t_{20}(0^\circ)$ is $-\sqrt{2}$, as predicted by perturbative QCD [44,46].

$$t_{22} = -434.5 \left(\frac{m}{Q} \right)^2 + [544703 + 872133(1 + \eta) \times \tan^2(\theta_e/2)] \left(\frac{m}{Q} \right)^4 + \mathcal{O}\left(\frac{m^6}{Q^6} \right). \quad (3.25)$$

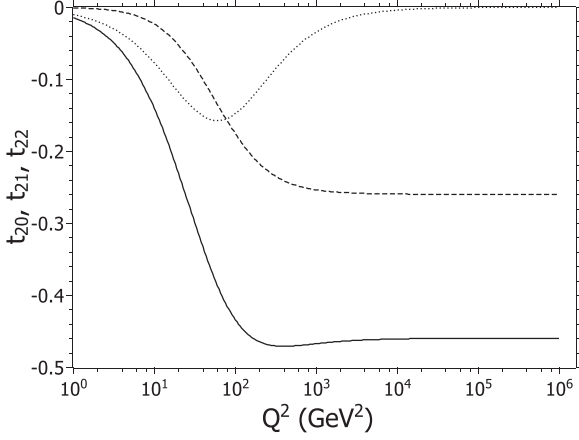
While at very large Q^2 , they are

$$t_{20} = -\sqrt{2} + 133 \tan^2(\theta_e/2) + 1064[1 + 2 \tan^2(\theta_e/2)] \left(\frac{m}{Q} \right)^2 + \mathcal{O}\left(\frac{m^4}{Q^4} \right), \quad (3.26)$$

$$t_{21} = 1217 \sec(\theta_e/2) \sin(\theta_e/2) [\tan^2(\theta_e/2) - 0.007972] + 114351[0.829452 - \cos \theta_e + 0.191998 \cos(2\theta_e) - 0.0214498 \cos(3\theta_e)] \sin^3 \theta_e \sin(\theta_e/2) \left(\frac{m}{Q} \right)^2 + \mathcal{O}\left(\frac{m^4}{Q^4} \right), \quad (3.27)$$

$$t_{22} = -[434.5 - 54508 \tan^2(\theta_e/2)] \left(\frac{m}{Q} \right)^2 + [544703 + 872133 \tan^2(\theta_e/2)] \left(\frac{m}{Q} \right)^4 + \mathcal{O}\left(\frac{m^6}{Q^6} \right). \quad (3.28)$$

The coefficients of nonleading terms are quite large. Thus, very large Q^2 is required for the leading term to be dominant, well beyond any available data. The limit of $-\sqrt{2}$ for t_{20} at $\theta_e = 0^\circ$ was an early prediction of perturbative QCD [44,46]. However, as argued elsewhere [43], this value is obtained only at very large Q^2 , and the value is quite different for small η . Figures 8 and 9 show plots of these observables at angles of 0° and 30° , respectively. We also compare with data [25] in Figs. 10–12. At these ‘small’ values of Q^2 , only t_{22} is consistent with data, something which is likely accidental with both data and model values near zero.

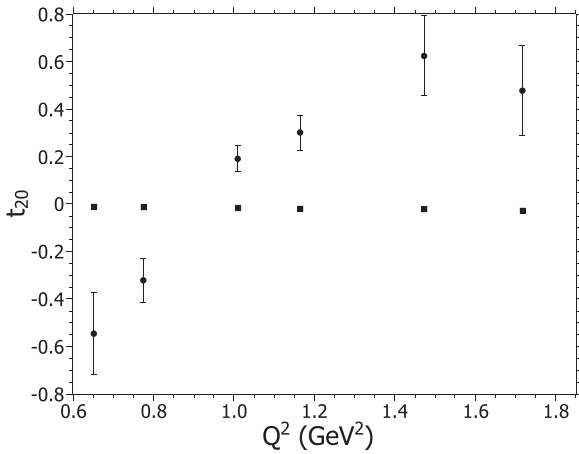
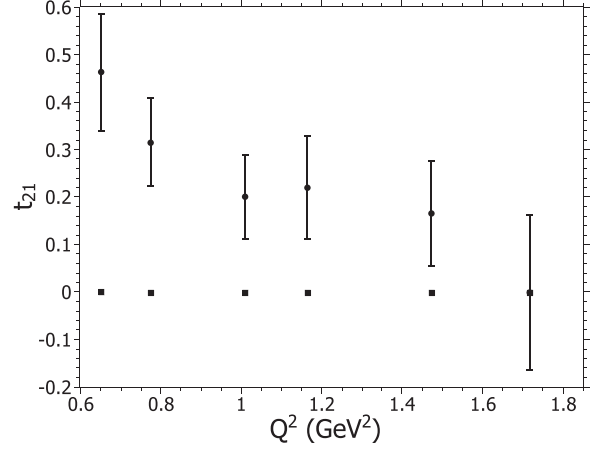

 FIG. 9. Same as Fig. 8 but for an angle of $\theta_e = 30^\circ$.

IV. PHOTODISINTEGRATION

In the photodisintegration of a deuteron, a real photon is absorbed and the two constituent nucleons emitted. This process is depicted in Fig. 13. The initial deuteron and photon four-momenta in the center-of-mass (c.m.) frame are $p = (E_d, 0, 0, -q_z)$ and $q = (q_z, 0, 0, q_z)$, where the incident photon is taken along the positive z axis. The final proton and neutron four-momenta are $p'_p = (E'_p, \vec{p}'_p)$ and $p'_n = (E'_n, \vec{p}'_n)$, with θ_p and ϕ_p the polar and azimuthal angles of the final proton. By ignoring the nucleon mass difference, we have $E'_p = E'_n$, because momentum conservation guarantees $\vec{p}'_p = -\vec{p}'_n$ in the c.m. frame.

In terms of the Mandelstam variable s , the c.m. energies and momenta are

$$\begin{aligned} E_d &= (s + 4m^2)/(2\sqrt{s}), & q_z &= (s - 4m^2)/(2\sqrt{s}), \\ E'_p &= \sqrt{s}/2, & |\vec{p}'_p| &= \sqrt{s - 4m^2}/2. \end{aligned} \quad (4.1)$$


 FIG. 10. Plots of the tensor polarization observable t_{20} of the deuteron from both data [25] (circles) and the model (squares) considered in the text. The angle θ_e varies and is as follows in order of increasing Q^2 : 35.6° , 33.4° , 29.8° , 27.3° , 23.0° , and 19.8° .

 FIG. 11. Same as Fig. 10 but for t_{21} .

The photon energy in the laboratory frame is $E_\gamma = (s - 4m^2)/4m$. We will work at large s , so that momentum transfers are large.

The standard definition of helicity amplitudes for photodisintegration is [47]

$$F_{i\pm} \equiv \epsilon_\nu(\lambda_\gamma) M^\nu(\lambda'_p, \lambda'_n, \lambda_d) \quad (4.2)$$

with ϵ the polarization vector for a photon with helicity λ_γ and M^ν given in Eq. (2.8). The index i is associated with particular helicity combinations as follows:

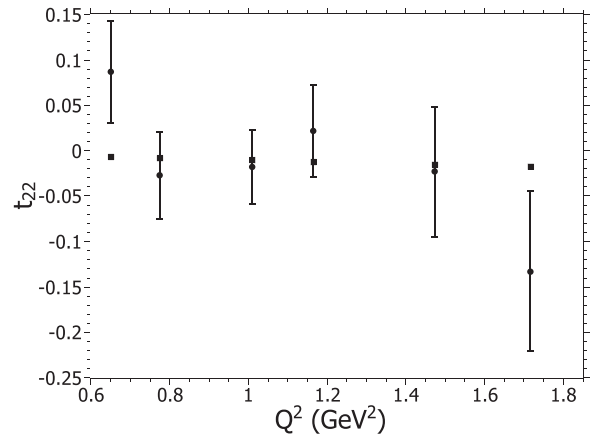
$$F_{1\pm} = \epsilon_\nu(1) M^\nu(\pm\frac{1}{2}, \pm\frac{1}{2}, 1), \quad F_{2\pm} = \epsilon_\nu(1) M^\nu(\pm\frac{1}{2}, \pm\frac{1}{2}, 0), \quad (4.3)$$

$$F_{3\pm} = \epsilon_\nu(1) M^\nu(\pm\frac{1}{2}, \pm\frac{1}{2}, -1), \quad F_{4\pm} = \epsilon_\nu(1) M^\nu(\pm\frac{1}{2}, \mp\frac{1}{2}, 1), \quad (4.4)$$

$$F_{5\pm} = \epsilon_\nu(1) M^\nu(\pm\frac{1}{2}, \mp\frac{1}{2}, 0), \quad F_{6\pm} = \epsilon_\nu(1) M^\nu(\pm\frac{1}{2}, \mp\frac{1}{2}, -1). \quad (4.5)$$

The other helicity combinations are related to these by parity.

The helicity amplitudes can be used to compute various polarization observables. The recoil-proton polarization P_y measures the asymmetry parallel/antiparallel to the normal


 FIG. 12. Same as Fig. 10 but for t_{22} .

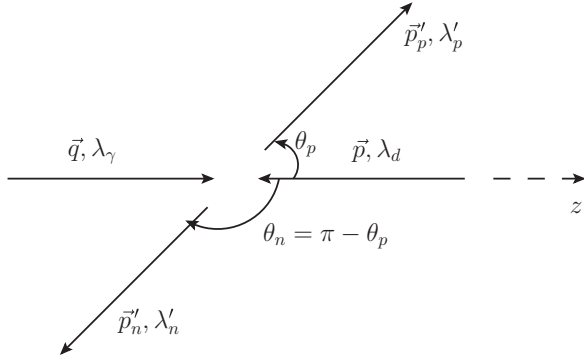


FIG. 13. Kinematics for deuteron photodisintegration in the c.m. frame, with \vec{q} the photon momentum and $\vec{p} = -\vec{q}$ the deuteron momentum. The final proton and neutron momenta are \vec{p}'_p and \vec{p}'_n . The λ 's are helicities. Coordinates are chosen such that the photon enters along the positive z direction and the azimuthal angle ϕ_p of the proton is zero.

$\hat{y} \propto \vec{q} \times \vec{p}'_p$ to the scattering plane

$$P_y = 2\text{Im} \sum_{i=1}^3 [F_{i+}^\dagger F_{i+3,-} + F_{i+3,+}^\dagger F_{i-}] / f(\theta_p), \quad (4.6)$$

where $f(\theta_p) = \sum_{i=1}^6 [|F_{i+}|^2 + |F_{i-}|^2]$ is the sum of all the helicity amplitudes squared. The transferred polarizations $C_{x'}$ and $C_{z'}$ measure asymmetries parallel/antiparallel to the $\hat{x}' \propto \vec{p}'_p \times \hat{y}$ and $\hat{z}' = \hat{p}'_p$ directions:

$$C_{x'} = 2\text{Re} \sum_{i=1}^3 [F_{i+}^\dagger F_{i+3,-} + F_{i+3,+}^\dagger F_{i-}] / f(\theta_p), \quad (4.7)$$

$$C_{z'} = \sum_{i=1}^6 [|F_{i+}|^2 - |F_{i-}|^2] / f(\theta_p). \quad (4.8)$$

The asymmetry Σ for linearly polarized photons is given by

$$\Sigma = -2\text{Re} \left[\sum_{\pm} (F_{1\pm}^\dagger F_{3\mp} - F_{4\pm}^\dagger F_{6\mp}) - F_{2+}^\dagger F_{2-} + F_{5+}^\dagger F_{5-} \right] / f(\theta_p). \quad (4.9)$$

Each observable is formed as a ratio, which sets aside questions of normalization.

Because we only need to consider photons with helicity +1, the polarization vector is always $\epsilon = -\frac{1}{\sqrt{2}}(0, 1, i, 0)$, relative to the momentum in the positive z direction. The final Dirac spinors are

$$u'_N = \frac{\not{p}'_N + m}{\sqrt{E'_N + m}} \begin{pmatrix} \phi^{(\lambda'_N)}(\hat{p}'_N) \\ 0 \end{pmatrix} \quad (4.10)$$

with $\theta_n = \pi - \theta_p$, $\phi_n = \phi_p + \pi = \pi$, and

$$\begin{aligned} \phi^{(1/2)}(\hat{p}'_N) &= \begin{pmatrix} \cos(\theta_N/2) \\ e^{i\phi_N} \sin(\theta_N/2) \end{pmatrix}, \\ \phi^{(-1/2)}(\hat{p}'_N) &= \begin{pmatrix} -e^{-i\phi_N} \sin(\theta_N/2) \\ \cos(\theta_N/2) \end{pmatrix}. \end{aligned} \quad (4.11)$$

With these spinors as input, the amplitudes $\epsilon_\nu M_X^\nu$ can be evaluated in terms of Dirac matrix and spinor products and then combined to construct the predefined amplitudes $F_{i\pm}$. At large s , these RNHA predictions for the helicity amplitudes reduce to

$$F_{1+} \sim 4 \frac{\sqrt{2}}{\sqrt{s}} \csc^2\left(\frac{\theta_p}{2}\right) G_{En}(\theta_p) G_{Ep}(\theta_p), \quad F_{1-} \sim 0, \quad (4.12)$$

$$F_{2+} \sim 2 \frac{m}{s} \cot^3\left(\frac{\theta_p}{2}\right) [G_{En}(\theta_p) G_{Mp}(\theta_p) - G_{Mn}(\theta_p) G_{Ep}(\theta_p)], \quad (4.13)$$

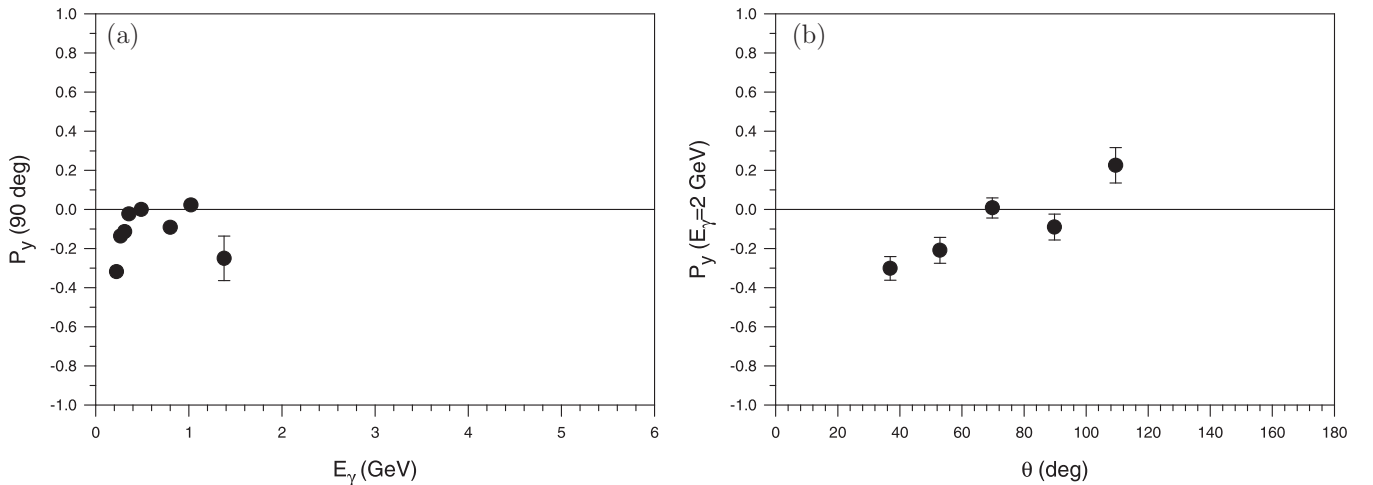
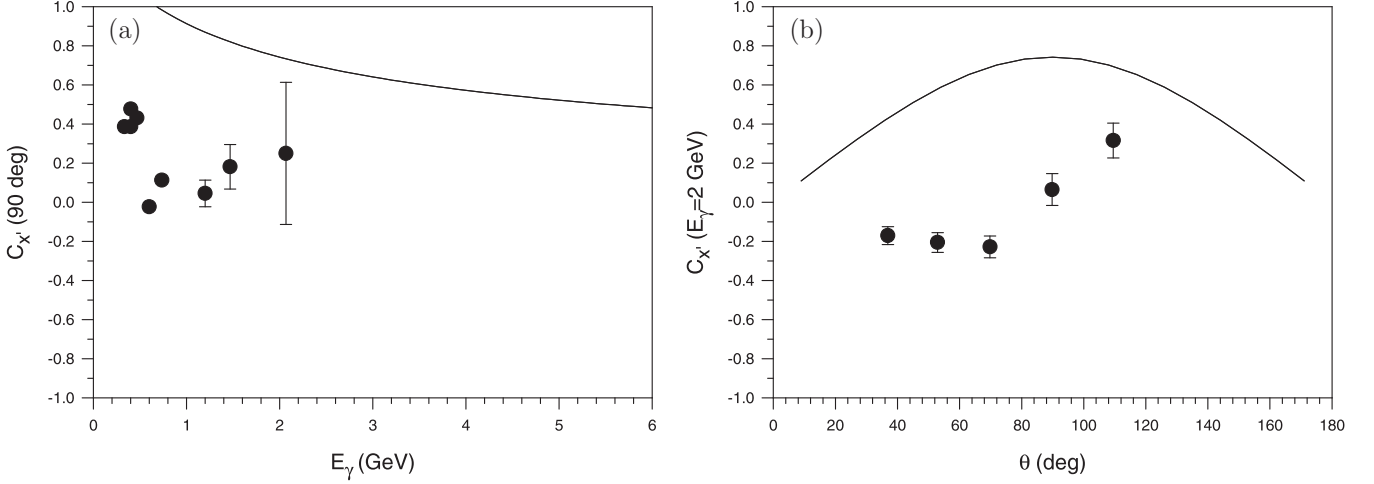


FIG. 14. Recoil proton polarization P_y as a function of (a) photon energy E_γ and (b) proton angle θ . For the latter, the photon energy is 2 GeV. The solid line is the RNHA prediction; the data points are from [48,49].


 FIG. 15. Same as Fig. 14 but for the transferred polarization C_x' .

$$F_{2-} \sim 2\frac{m}{s} \cot\left(\frac{\theta_p}{2}\right) [G_{Mn}(\theta_p)G_{Ep}(\theta_p) - G_{En}(\theta_p)G_{Mp}(\theta_p)],$$

$$F_{3+} \sim 0, \quad F_{3-} \sim 0, \quad (4.14)$$

$$F_{4+} \sim -4\sqrt{2}\frac{m}{s} \cot\left(\frac{\theta_p}{2}\right) G_{Mn}(\theta_p)G_{Ep}(\theta_p),$$

$$F_{4-} \sim 4\sqrt{2}\frac{m}{s} \cot\left(\frac{\theta_p}{2}\right) G_{En}(\theta_p)G_{Mp}(\theta_p), \quad (4.15)$$

$$F_{5+} \sim \frac{2}{\sqrt{s}} \cot^2\left(\frac{\theta_p}{2}\right) G_{En}(\theta_p)G_{Ep}(\theta_p),$$

$$F_{5-} \sim \frac{2}{\sqrt{s}} G_{En}(\theta_p)G_{Ep}(\theta_p), \quad (4.16)$$

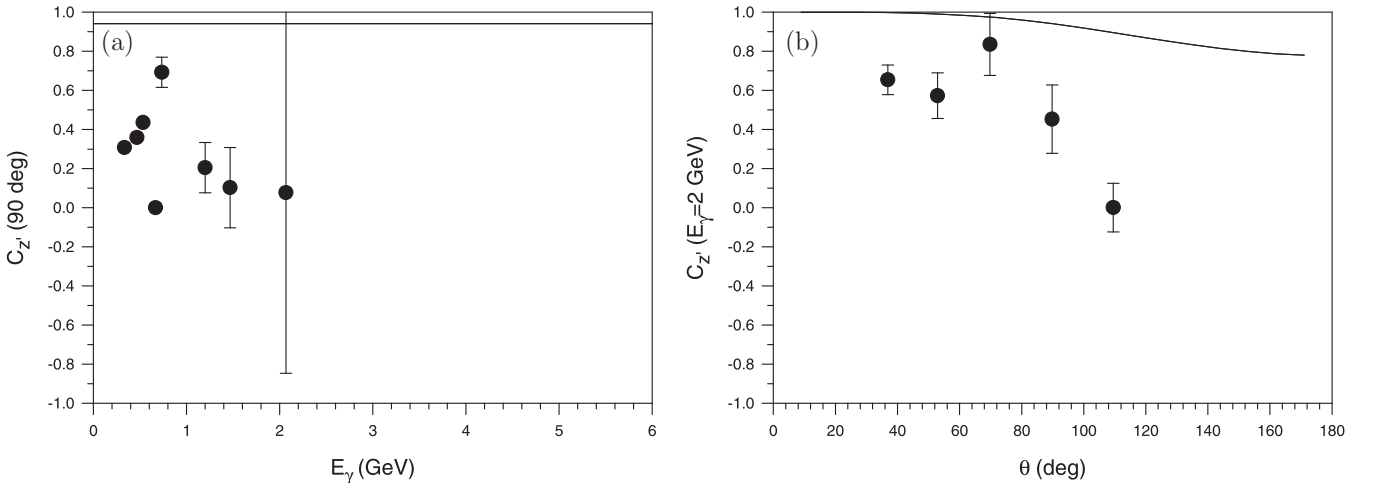
$$F_{6+} \sim 4\sqrt{2}\frac{m}{s} \cot^3\left(\frac{\theta_p}{2}\right) G_{En}(\theta_p)G_{Mp}(\theta_p),$$

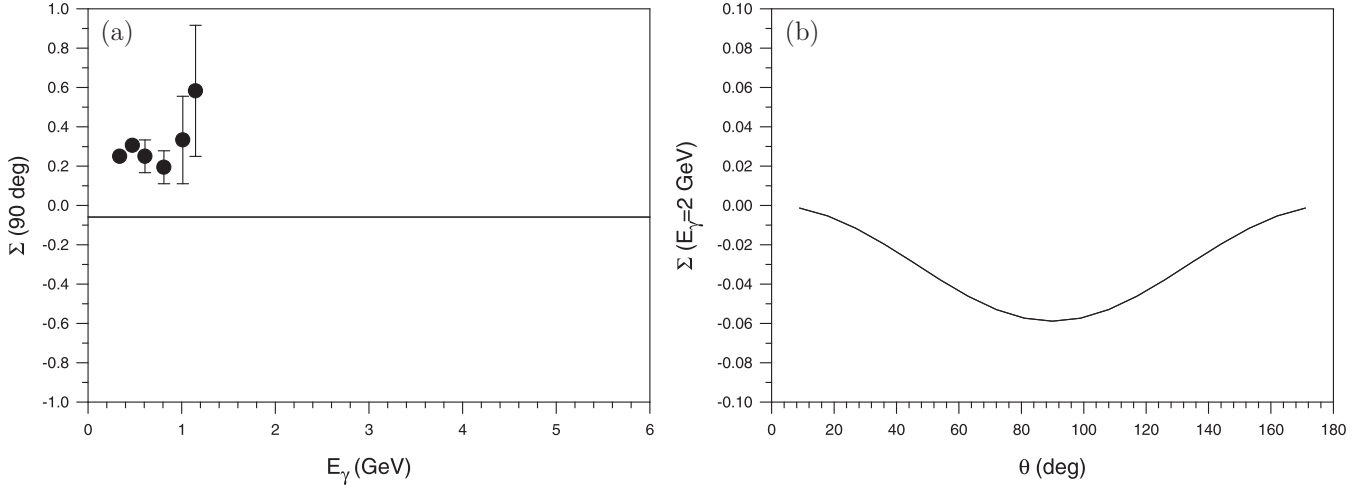
$$F_{6-} \sim -4\sqrt{2}\frac{m}{s} \cot\left(\frac{\theta_p}{2}\right) G_{Mn}(\theta_p)G_{Ep}(\theta_p). \quad (4.17)$$

Here $G_{XN}(\theta_p)$ represents $G_{XN}(Q^2)$ with $Q^2 = mE_\gamma[1 - \sqrt{\frac{E_\gamma}{m+E_\gamma}} \cos\theta_p]$. From these we can calculate the various observables. Plots of the results and recent data [48–50] are given in Figs. 14–17. Because the tree-level amplitudes are real, P_y is automatically zero. That C_x' is of order m/\sqrt{s} , rather than zero, is a correction to hadron helicity conservation [51]. Also, we find the asymmetry $\Sigma(90^\circ)$ to be approximately -0.06 , rather than the nominal expectation [52] of -1 . In general, the trends with photon energy seem to be modestly consistent with data.

V. ELECTRODISINTEGRATION

The kinematics of the electrodisintegration process are shown in Fig. 18. The initial (final) momentum and helicity of the electron are p_e (p_e') and λ_e (λ_e'). The intermediate photon carries four-momentum q . The azimuthal angle ϕ_p of the proton measures the rotation of the hadronic reaction plane relative to the electron scattering plane.


 FIG. 16. Same as Fig. 15 but for C_z' .

FIG. 17. Same as Fig. 14 but for the asymmetry Σ . The data points are from [50].

In the laboratory frame, with the z axis taken along the photon three-momentum and the electron mass neglected, the initial and final electron four-momenta are

$$\begin{aligned} p_e &= (E_e, E_e \sin \theta_e, 0, E_e \cos \theta_e), \\ p'_e &= (E'_e, E'_e \sin \theta'_e, 0, E'_e \cos \theta'_e) \end{aligned} \quad (5.1)$$

with E'_e and $\tilde{\theta} = \theta'_e - \theta_e$, the angle of the scattered electron to the beam direction, being measured. The photon four-momentum $q = (E_\gamma, 0, 0, q_z)$ is just $p_e - p'_e$, which yields

$$\begin{aligned} Q^2 &\equiv -q^2 = 2E_e E'_e (1 - \cos \tilde{\theta}), \\ E_\gamma &= E_e - E'_e, \quad q_z = \sqrt{E_\gamma^2 + Q^2}. \end{aligned} \quad (5.2)$$

The deuteron four-momentum is $p = (m_d = 2m, 0, 0, 0)$, and in the zero-binding limit, the initial proton and neutron four-momenta are $p_p = p_n = (m, 0, 0, 0)$. The final nucleon four-momenta are

$$\begin{aligned} p'_p &= (E'_p = \sqrt{\vec{p}'_p{}^2 + m^2}, |\vec{p}'_p| \sin \theta_p \cos \phi_p, |\vec{p}'_p| \sin \theta_p \sin \phi_p, \\ &|\vec{p}'_p| \cos \theta_p), \end{aligned} \quad (5.3)$$

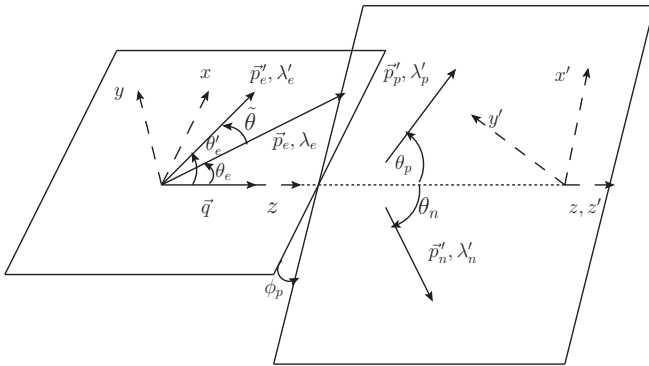


FIG. 18. Kinematics for deuteron electrodisintegration. The unprimed axes are defined relative to the electron scattering plane, and the primed axes relative to the final nucleon momenta. The final proton momentum has polar angle θ_p and azimuthal angle ϕ_p relative to the unprimed frame.

$$\begin{aligned} p'_n &= (E'_n = \sqrt{\vec{p}'_n{}^2 + m^2}, -|\vec{p}'_n| \sin \theta_n \cos \phi_p, \\ &-|\vec{p}'_n| \sin \theta_n \sin \phi_p, |\vec{p}'_n| \cos \theta_n). \end{aligned} \quad (5.4)$$

Within the one-photon-exchange approximation, the scattering amplitude is proportional to

$$M_{ed}(\lambda'_p, \lambda'_n, \lambda'_e; \lambda_d, \lambda_e) = \bar{u}'_e \gamma_\mu u_e \frac{D_{\mu\nu}}{q^2} M^\nu(\lambda'_p, \lambda'_n, \lambda_d) \quad (5.5)$$

with u_e (u'_e) the initial (final) spinor of the electron and M^ν given in Eq. (2.8). The numerator of the photon propagator is the sum over photon polarizations

$$D_{\mu\nu} = \sum_{\lambda=-1}^1 (-1)^\lambda \epsilon_\mu^*(\lambda) \epsilon_\nu(\lambda). \quad (5.6)$$

The polarization four-vectors are⁴

$$\epsilon(\pm 1) = \mp \frac{1}{\sqrt{2}} (0, 1, \pm i, 0), \quad \epsilon(0) = (q_z/Q, 0, 0, E_\gamma/Q) \quad (5.7)$$

relative to the photon four-momentum $q = (E_\gamma, 0, 0, q_z)$. Polarization observables [5–15] can then be computed from these helicity amplitudes.

In keeping with the notation of [6,7] and [15], the differential cross section for electrodisintegration, summed over the final electron and neutron helicities in the laboratory frame, is [14,15]⁵

$$\begin{aligned} d\sigma &\equiv \frac{d\sigma^5}{dE' d\Omega'_e d\Omega'_p} \\ &= \frac{m_p m_n |\vec{p}'_p|}{16\pi^3 m_d} \frac{\sigma_{\text{Mott}}}{f_{\text{rec}}} [\nu_L R_L + \nu_T R_T + \nu_{TT} R_{TT} + \nu_{LT} R_{LT} \\ &\quad + 2\lambda_e \nu_{LT'} T_{LT'} + 2\lambda_e \nu_{T'} R_{T'}], \end{aligned} \quad (5.8)$$

⁴In the hadronic c.m. frame, the longitudinal polarization vector is $\epsilon(0) = (q_z/Q, 0, 0, E'_\gamma/Q)$.

⁵In [6], h is $2\lambda_e$ but in [15], h is just λ_e , which leads to additional factors of 2.

where Ω'_e (Ω'_p) is the solid angle of the scattered electron (proton), σ_{Mott} is the Mott cross section, $f_{\text{rec}} = |1 + (E_\gamma |\vec{p}'_p| - E'_p q_z \cos \theta_p) / (m_d |\vec{p}'_p|)|$ is the laboratory recoil factor,

$$\begin{aligned} \nu_L &= \frac{Q^4}{q_z^4}, & \nu_T &= \frac{Q^2}{2q_z^2} + \tan^2 \frac{\tilde{\theta}}{2}, & \nu_{TT} &= \frac{Q^2}{2q_z^2}, \\ \nu_{LT} &= \frac{Q^2}{\sqrt{2}q_z^2} \sqrt{\frac{Q^2}{q_z^2} + \tan^2 \frac{\tilde{\theta}}{2}}, \\ \nu_{LT'} &= -\frac{Q^2}{\sqrt{2}q_z^2} \tan \frac{\tilde{\theta}}{2}, & \nu_{T'} &= \tan \frac{\tilde{\theta}}{2} \sqrt{\frac{Q^2}{q_z^2} + \tan^2 \frac{\tilde{\theta}}{2}}, \end{aligned} \quad (5.9)$$

and $\tilde{\theta} = \theta'_e - \theta_e$ is the angle between the incoming and outgoing electron. The response functions R_X depend upon the hadronic helicity amplitudes and the azimuthal angle ϕ_p of the hadronic scattering plane. The subscripts refer to the polarization of the intermediate photon, which enters on substitution of the polarization expansion (5.6) for the numerator of the photon propagator in the hadronic amplitude (5.5). The amplitude then decomposes into separate leptonic and hadronic factors

$$\begin{aligned} M_{ed}(\lambda'_p, \lambda'_n, \lambda'_e; \lambda_d, \lambda_e) &= - \sum_{\lambda=-1}^1 \bar{u}'_e \not{\epsilon}^*(\lambda) u_e \frac{(-1)^\lambda}{Q^2} \epsilon_\nu(\lambda) \\ &\times M^\nu(\lambda'_p, \lambda'_n, \lambda_d). \end{aligned} \quad (5.10)$$

The leptonic factors give rise to the ν_X coefficients, and the hadronic factors to the response functions in the square of the amplitude used to construct the cross section [15]. The subscript $L(T)$ indicates a purely longitudinal (transverse) contribution, while LT is a cross term between longitudinal and transverse photon helicities. The TT subscript marks a cross term between different transverse helicities. A prime indicates a different combination of transverse helicities.

The response functions are computed from components of the hadronic tensor

$$\begin{aligned} w_{\lambda', \lambda} &= \frac{2}{3} \sum_{\lambda''_p, \lambda''_n, \lambda''_d, \lambda''_e} \epsilon_\nu^*(\lambda') M^{\nu*}(\lambda''_p, \lambda''_n, \lambda''_d) \rho_{\lambda''_p, \lambda''_e}^p \epsilon_\mu(\lambda) \\ &\times M^\mu(\lambda'_p, \lambda'_n, \lambda_d) \rho_{\lambda''_d, \lambda''_e}^d \end{aligned} \quad (5.11)$$

with ρ^p (ρ^d) the density matrix for the proton (deuteron) helicity state. We construct these in the xyz coordinate system of the electron scattering plane. The particular components are [6]

$$\begin{aligned} R_L &= w_{0,0}, & R_T &= w_{1,1} + w_{-1,-1}, & R_{T'} &= w_{1,1} - w_{-1,-1}, \\ R_{TT} &= 2\text{Re}w_{1,-1}, & R_{LT} &= -2\text{Re}[w_{0,1} - w_{0,-1}], \\ R_{LT'} &= -2\text{Re}[w_{0,1} + w_{0,-1}]. \end{aligned} \quad (5.12)$$

For an unpolarized target, the deuteron density matrix is proportional to the identity, $\rho^d = \frac{1}{3}I$; similarly, if the proton helicity is not detected, $\rho^p = \frac{1}{2}I$. We then have the

unpolarized cross section [6]

$$\begin{aligned} d\sigma_{\text{unpol}} &= \frac{m_p m_n |\vec{p}'_p|}{16\pi^3 m_d} \frac{\sigma_{\text{Mott}}}{f_{\text{rec}}} \sigma_0, \\ \sigma_0 &\equiv \nu_L R_L^U + \nu_T R_T^U + \nu_{TT} R_{TT}^U + \nu_{LT} R_{LT}^U, \end{aligned} \quad (5.13)$$

where the R_X^U are computed with the simple density matrices. These are then computable in our model, with the basic computation being the evaluation of $\epsilon(\lambda_\gamma)_\mu M^\mu$, which differs from the photodisintegration calculation in only two ways: Q^2 is not zero and λ_γ ranges over all three possibilities.

The unpolarized response functions $R_{LT'}^U$ and $R_{T'}^U$ are identically zero. With ρ^d replaced by $\frac{1}{3}I$ and the form (5.7) of the polarization vectors taken into account, $\text{Re}w(0, 1)$ is just the negative of $\text{Re}w(0, -1)$, and $w_{1,1}$ is equal to $w_{-1,-1}$. Thus, the inputs to $R_{LT'}^U$ and $R_{T'}^U$, as given in Eq. (5.12), immediately cancel.

The recent $ed \rightarrow e'pn$ experiment at JLab [17] does not include polarization but does begin to reach momentum transfers sufficient to consider the RNHA approach. Once polarization data is available, the expressions developed here and in the Appendix can be compared.

VI. SUMMARY

We have extended the reduced nuclear amplitude approach [1,2] to helicity amplitudes and applied this model to analysis of elastic electron-deuteron scattering, deuteron photodisintegration, and deuteron electrodisintegration. These are just examples of the approach, which is generally applicable to exclusive nuclear processes. The primary limitation is that, for any process, the net momentum transfer to every nucleon must be large; therefore, as the number of nucleons increases, the required beam energy can increase dramatically. The primary gain is precocious scaling in the dependence on momentum transfer. What the model (or the original RNA approach) does not provide, though, is an overall normalization; comparisons must be made in terms of ratios.

By considering helicity amplitudes, many more quantities can be studied, including polarization dependence. All three of the deuteron's electromagnetic form factors can be calculated and from there various elastic scattering observables can be constructed. In Sec. III we considered the standard structure functions A and B as well as the tensor polarizations t_{2m} . Generally, the model implies the need for momentum transfers larger than one would have hoped for seeing simple perturbative QCD scaling. However, our results do imply that the deuteron structure function B is a good place to look, above a transfer of 10 GeV².

The RNHA results for polarization observables in deuteron photodisintegration, considered in Sec. IV, are somewhat consistent with experiment. In particular, our result for the asymmetry Σ , with a value of $\Sigma(90^\circ) \simeq -0.06$, is much better than the value of -1 originally expected [52]. Higher photon energies would, of course, be useful.

We have also constructed the RNHA framework for analysis of deuteron electrodisintegration, in Sec. V. This stands

ready for comparison with experiment when data is available at sufficient energies. One aspect that does remain is to consider polarization of the outgoing proton, in addition to polarization of the beam and target.

Other processes that one might consider include deeply virtual Compton scattering on the deuteron, pion photoproduction on the deuteron [3], and photodisintegration of ${}^3\text{He}$ [4]. In each case, our approach can provide not only information about helicity amplitudes but also an analysis of nonleading momentum transfer dependence with respect to

the onset of perturbative QCD scaling. We look forward to experiments at larger momentum transfers for all of these processes.

ACKNOWLEDGMENTS

This work began in conversations with S. J. Brodsky and D.-S. Hwang. Some calculations were checked by W. Miller and C. Salvesson. Diagrams were drawn with use of Jaxo-Draw [53].

APPENDIX: ELECTRODISINTEGRATION WITH POLARIZATION

If we consider polarization for the beam and the target,⁶ the proton density matrix is still just $\rho^p = \frac{1}{2}I$, but the deuteron density matrix in the xyz frame is [6]

$$\rho^d = \frac{1}{3} \begin{pmatrix} 1 + \sqrt{\frac{3}{2}}T_{10} + \frac{1}{\sqrt{2}}T_{20} & -\sqrt{\frac{3}{2}}(T_{11}^* + T_{21}^*) & \sqrt{3}T_{22}^* \\ -\sqrt{\frac{3}{2}}(T_{11} + T_{21}) & 1 - \sqrt{2}T_{20} & -\sqrt{\frac{3}{2}}(T_{11}^* - T_{21}^*) \\ \sqrt{3}T_{22} & -\sqrt{\frac{3}{2}}(T_{11} - T_{21}) & 1 - \sqrt{\frac{3}{2}}T_{10} + \frac{1}{\sqrt{2}}T_{20} \end{pmatrix}. \quad (\text{A1})$$

For a target polarization defined relative to the beam direction, rather than the xyz system used above, the tensor polarization coefficients T_{JM} are related to the coefficients \tilde{T}_{JM} defined relative to the beam [6]. If only \tilde{T}_{10} and \tilde{T}_{20} are nonzero,⁷ the nonzero T_{JM} are

$$T_{10} = \cos \tilde{\theta} \tilde{T}_{10}, \quad T_{11} = -\frac{1}{\sqrt{2}} \sin \tilde{\theta} \tilde{T}_{10}, \quad T_{20} = \frac{1}{4}(1 + 3 \cos 2\tilde{\theta})\tilde{T}_{20}, \quad T_{21} = -\sqrt{\frac{3}{8}} \sin 2\tilde{\theta} \tilde{T}_{20}, \quad T_{22} = \sqrt{\frac{3}{32}}(1 - \cos 2\tilde{\theta})\tilde{T}_{20}. \quad (\text{A2})$$

The density matrix can then be written as

$$\rho^d = (\frac{1}{3}I + \tilde{T}_{10}\rho^{dV} + \tilde{T}_{20}\rho^{dT}), \quad (\text{A3})$$

where

$$\rho^{dV} = \frac{1}{3} \begin{pmatrix} \sqrt{\frac{3}{2}} \cos \tilde{\theta} & \frac{\sqrt{3}}{2} \sin \tilde{\theta} & 0 \\ \frac{\sqrt{3}}{2} \sin \tilde{\theta} & 0 & \frac{\sqrt{3}}{2} \sin \tilde{\theta} \\ 0 & \frac{\sqrt{3}}{2} \sin \tilde{\theta} & -\sqrt{\frac{3}{2}} \cos \tilde{\theta} \end{pmatrix} \quad (\text{A4})$$

and

$$\rho^{dT} = \frac{1}{3} \begin{pmatrix} \frac{1}{4\sqrt{2}}(1 + 3 \cos 2\tilde{\theta}) & \frac{3}{4} \sin 2\tilde{\theta} & \frac{3}{\sqrt{32}}(1 - \cos 2\tilde{\theta}) \\ \frac{3}{4} \sin 2\tilde{\theta} & -\frac{1}{2\sqrt{2}}(1 + 3 \cos 2\tilde{\theta}) & -\frac{3}{4} \sin 2\tilde{\theta} \\ \frac{3}{\sqrt{32}}(1 - \cos 2\tilde{\theta}) & -\frac{3}{4} \sin 2\tilde{\theta} & \frac{1}{4\sqrt{2}}(1 + 3 \cos 2\tilde{\theta}) \end{pmatrix}. \quad (\text{A5})$$

The response functions can then be separated into unpolarized, vector, and tensor contributions as $R_X = R_X^U + \tilde{T}_{10}R_X^V + \tilde{T}_{20}R_X^T$, with R_X^U , R_X^V , and R_X^T computed with ρ^d replaced by $\frac{1}{3}I$, ρ^{dV} , and ρ^{dT} , respectively.

With $d\sigma_{\text{unpol}}$ defined as the unpolarized cross section, given in Eq. (5.13), the full cross section can be written as

$$d\sigma = [1 + \tilde{T}_{10}(A_d^V + 2\lambda_e A_{ed}^V) + \tilde{T}_{20}(A_d^T + 2\lambda_e A_{ed}^T)]d\sigma_{\text{unpol}}, \quad (\text{A6})$$

in terms of the single and double asymmetries

$$A_d^V = [v_L R_L^V + v_T R_T^V + v_{TT} R_{TT}^V + v_{LT} R_{LT}^V]/\sigma_0, \quad (\text{A7})$$

$$A_{ed}^V = [v_{LT'} R_{LT'}^V + v_{T'} R_{T'}^V]/\sigma_0, \quad (\text{A8})$$

⁶For discussion of a polarized outgoing proton, see [7] and [15].

⁷The spherical tensor moments are related to the Cartesian tensor moments as $\tilde{T}_{10} = \sqrt{\frac{3}{2}}P_z$ and $\tilde{T}_{20} = \frac{1}{\sqrt{2}}P_{zz}$.

$$A_d^T = [\nu_L R_L^T + \nu_T R_T^T + \nu_{TT} R_{TT}^T + \nu_{LT} R_{LT}^T] / \sigma_0, \quad (\text{A9})$$

$$A_{ed}^T = [\nu_{LT'} R_{LT'}^T + \nu_{T'} R_{T'}^T] / \sigma_0. \quad (\text{A10})$$

For a recent summary of data, see [54].

-
- [1] S. J. Brodsky and B. T. Chertok, Deuteron Form Factor and the Short-Distance Behavior of the Nuclear Force, *Phys. Rev. Lett.* **37**, 269 (1976); The asymptotic form-factors of hadrons and nuclei and the continuity of particle and nuclear dynamics, *Phys. Rev. D* **14**, 3003 (1976).
- [2] S. J. Brodsky and J. R. Hiller, Reduced nuclear amplitudes in quantum chromodynamics, *Phys. Rev. C* **28**, 475 (1983); Erratum: Reduced nuclear amplitudes in quantum chromodynamics, **30**, 412(E) (1984).
- [3] S. J. Brodsky, J. R. Hiller, C. R. Ji, and G. A. Miller, Perturbative QCD and factorization of coherent pion photoproduction on the deuteron, *Phys. Rev. C* **64**, 055204 (2001).
- [4] S. J. Brodsky, L. Frankfurt, R. A. Gilman, J. R. Hiller, G. A. Miller, E. Piasetzky, M. Sargsian, and M. Strikman, Hard photodisintegration of a proton pair in ^3He , *Phys. Lett. B* **578**, 69 (2004).
- [5] S. Jeschonnek and J. W. Van Orden, Modeling quark-hadron duality in polarization observables, *Phys. Rev. D* **71**, 054019 (2005); A new calculation for $D(e, e'p)n$ at GeV energies, *Phys. Rev. C* **78**, 014007 (2008).
- [6] S. Jeschonnek and J. W. Van Orden, Target polarization for $^2\text{H}(e, e'p)$ at GeV energies, *Phys. Rev. C* **80**, 054001 (2009).
- [7] S. Jeschonnek and J. W. Van Orden, Ejectile polarization for $^2\text{H}(e, e'\bar{p})$ at GeV energies, *Phys. Rev. C* **81**, 014008 (2010).
- [8] W. P. Ford, S. Jeschonnek and J. W. Van Orden, $^2\text{H}(e, e'p)$ observables using a Regge model parameterization of final state interactions, *Phys. Rev. C* **87**, 054006 (2013); Momentum distributions for $^2\text{H}(e, e'p)$, **90**, 064006 (2014); S. Jeschonnek and J. W. Van Orden, Factorization breaking of A_d^T for polarized deuteron targets in a relativistic framework, *ibid.* **95**, 044001 (2017).
- [9] J. M. Laget, The electro-disintegration of few body systems revisited, *Phys. Lett. B* **609**, 49 (2005).
- [10] C. Ciofi delgi Atti and L. P. Kaptari, A Non Factorized Calculation of the Process $^3\text{He}(e, e'p)^2\text{H}$ at Medium Energies, *Phys. Rev. Lett.* **100**, 122301 (2008).
- [11] M. M. Sargsian, Large Q^2 electrodisintegration of the deuteron in virtual nucleon approximation, *Phys. Rev. C* **82**, 014612 (2010).
- [12] H. Arenhövel, W. Leidemann, and E. L. Tomusiak, General formulae for polarization observables in deuteron electrodisintegration and linear relations, *Few Body Syst.* **15**, 109 (1993); General survey of polarization observables in deuteron electrodisintegration, *Eur. Phys. J. A* **23**, 147 (2005).
- [13] G. I. Gakh, A. P. Rekalov, and E. Tomasi-Gustafsson, Relativistically invariant analysis of polarization effects in exclusive deuteron electrodisintegration process, *Ann. Phys. (NY)* **319**, 150 (2005).
- [14] A. S. Raskin and T. W. Donnelly, Polarization in coincidence electron scattering from nuclei, *Ann. Phys. (NY)* **191**, 78 (1989).
- [15] V. Dmitrasinovic and F. Gross, A Comment on general formulae for polarization observables in deuteron electrodisintegration and linear relations, *Few-Body Syst.* **20**, 41 (1996); Polarization observables in deuteron photodisintegration and electrodisintegration, *Phys. Rev. C* **40**, 2479 (1989); Erratum: Polarization observables in deuteron photodisintegration and electrodisintegration, **43**, 1495(E) (1991).
- [16] C. E. Carlson, J. R. Hiller, and R. J. Holt, Relativistic QCD view of the deuteron, *Annu. Rev. Nucl. Part. Sci.* **47**, 395 (1997).
- [17] C. Yero *et al.*, Probing the Deuteron at Very Large Internal Momenta, *Phys. Rev. Lett.* **125**, 262501 (2020).
- [18] C. Yero, Cross section measurements of deuteron electrodisintegration at very high recoil momenta and large 4-momentum transfers (Q^2), Ph.D. thesis, Florida International University, Miami, Florida, 2020, [arXiv:2009.11343](https://arxiv.org/abs/2009.11343) [nucl-ex].
- [19] W. Boeglin and M. Sargsian, Modern studies of the deuteron: From the lab frame to the light front, *Int. J. Mod. Phys. E* **24**, 1530003 (2015).
- [20] R. A. Gilman and F. Gross, Electromagnetic structure of the deuteron, *J. Phys. G: Nucl. Part. Phys.* **28**, R37 (2002).
- [21] R. G. Arnold *et al.*, Measurement of the Electron-Deuteron Elastic-Scattering Cross Section in the Range $0.8 \leq q^2 \leq 6 \text{ GeV}^2$, *Phys. Rev. Lett.* **35**, 776 (1975).
- [22] P. E. Bosted *et al.*, Measurements of the deuteron and proton magnetic form factors at large momentum transfers, *Phys. Rev. C* **42**, 38 (1990).
- [23] D. Abbott *et al.*, Precise Measurement of the Deuteron Elastic Structure Function $A(Q^2)$, *Phys. Rev. Lett.* **82**, 1379 (1999).
- [24] L. C. Alexa *et al.*, Measurements of the Deuteron Elastic Structure Function $A(Q^2)$ for $0.7 \leq Q^2 \leq 6.0 \text{ (GeV/c)}^2$ at Jefferson Laboratory, *Phys. Rev. Lett.* **82**, 1374 (1999).
- [25] D. Abbott *et al.*, Measurement of Tensor Polarization in Elastic Electron-Deuteron Scattering at Large Momentum Transfer, *Phys. Rev. Lett.* **84**, 5053 (2000).
- [26] C. Bochna *et al.*, Measurements of Deuteron Photodisintegration up to 4.0 GeV, *Phys. Rev. Lett.* **81**, 4576 (1998).
- [27] E. C. Schulte *et al.*, Measurement of the High Energy Two-Body Deuteron Photodisintegration Differential Cross Section, *Phys. Rev. Lett.* **87**, 102302 (2001).
- [28] E. C. Schulte *et al.*, High energy angular distribution measurements of the exclusive deuteron photodisintegration reaction, *Phys. Rev. C* **66**, 042201 (2002).
- [29] M. Mirazita *et al.*, Complete angular distribution measurements of two-body deuteron photodisintegration between 0.5 and 3 GeV, *Phys. Rev. C* **70**, 014005 (2004).
- [30] W.-J. Kasdorp *et al.*, Deuteron electrodisintegration at high missing momenta, *Few-Body Syst.* **25**, 115 (1998).
- [31] P. E. Ulmer *et al.*, $^2\text{H}(e, e'p)n$ Reaction at High Recoil Momenta, *Phys. Rev. Lett.* **89**, 062301 (2002).
- [32] W. U. Boeglin *et al.*, Probing the High Momentum Component

- of the Deuteron at High Q^2 , *Phys. Rev. Lett.* **107**, 262501 (2011).
- [33] K. S. Egiyan *et al.*, Experimental Study of Exclusive $^3\text{H}(e, e'p)n$ Reaction Mechanisms at High Q^2 , *Phys. Rev. Lett.* **98**, 262502 (2007).
- [34] S. J. Brodsky, C.-R. Ji, and G. P. Lepage, Quantum Chromodynamic Predictions for the Deuteron Form Factor, *Phys. Rev. Lett.* **51**, 83 (1983).
- [35] M. M. Sargsian, Polarization observables in hard rescattering mechanism of deuteron photodisintegration, *Phys. Lett. B* **587**, 41 (2004).
- [36] V. Yu. Grishina *et al.*, Forward-backward angle asymmetry and polarization observables in high-energy deuteron photodisintegration, *Eur. Phys. J. A* **19**, 117 (2004).
- [37] V. A. Knyr, V. G. Neudachin, and N. A. Khokhlov, Description of polarization data for deuteron photodisintegration at photon energies in the range $E_\gamma = 1.5\text{-}2.5$ GeV on the basis of the Moscow potential of NN interaction, *Phys. At. Nucl.* **70**, 2152 (2007).
- [38] N. Huseynova, S. Mamedov, and J. Samadov, Deuteron electromagnetic form factors and tensor polarization observables in the framework of the hard-wall AdS/QCD model, *Chin. Phys. C* **47**, 013104 (2023).
- [39] T. Gutsche, V. E. Lyubovitskij, I. Schmidt and A. Vega, Nuclear physics in soft-wall AdS/QCD: Deuteron electromagnetic form factors, *Phys. Rev. D* **91**, 114001 (2015); T. Gutsche, V. E. Lyubovitskij and I. Schmidt, Deuteron electromagnetic structure functions and polarization properties in soft-wall AdS/QCD, *ibid.* **94**, 116006 (2016).
- [40] S. Galster *et al.*, Elastic electron-deuteron scattering and the electric neutron form factor at four-momentum transfers $5\text{ fm}^{-2} < q^2 < 14\text{ fm}^{-2}$, *Nucl. Phys. B* **32**, 221 (1971); M. A. Preston and R. K. Bhaduri, *Structure of the Nucleon* (Addison-Wesley, Reading, MA, 1975).
- [41] M. D. Scadron, *Advanced Quantum Theory and Its Applications Through Feynman Diagrams*, (Springer, Berlin, 1991).
- [42] R. G. Arnold, C. E. Carlson, and F. Gross, Elastic electron-deuteron scattering at high-energy, *Phys. Rev. C* **21**, 1426 (1980).
- [43] S. J. Brodsky and J. R. Hiller, Universal properties of the electromagnetic interactions of spin one systems, *Phys. Rev. D* **46**, 2141 (1992).
- [44] C. E. Carlson and F. Gross, Distinctive Signatures for Quantum Chromodynamics in Nuclear Physics, *Phys. Rev. Lett.* **53**, 127 (1984).
- [45] S. D. Drell and T. M. Yan, Connection of Elastic Electromagnetic Nucleon Form-Factors at Large Q^2 and Deep Inelastic Structure Functions Near Threshold, *Phys. Rev. Lett.* **24**, 181 (1970).
- [46] R. Dymarz and F. C. Khanna, Tensor Polarization of the Deuteron in Elastic e^-D Scattering, *Phys. Rev. Lett.* **56**, 1448 (1986).
- [47] V. P. Barannik *et al.*, Proton polarization in deuteron disintegration by linearly polarized photons and dibaryon resonances, *Nucl. Phys. A* **451**, 751 (1986).
- [48] K. Wijesooriya *et al.*, Polarization Measurements in High-Energy Deuteron Photodisintegration, *Phys. Rev. Lett.* **86**, 2975 (2001).
- [49] X. Jiang *et al.*, Recoil-Proton Polarization in High-Energy Deuteron Photodisintegration with Circularly Polarized Photons, *Phys. Rev. Lett.* **98**, 182302 (2007).
- [50] F. Adamian *et al.*, Measurement of the cross-section asymmetry of deuteron photodisintegration process by linearly polarized photons in the energy range $E_\gamma = 0.8$ GeV to 1.6 GeV, *Eur. Phys. J. A* **8**, 423 (2000).
- [51] S. J. Brodsky and G. P. Lepage, Helicity selection rules and tests of gluon spin in exclusive QCD processes, *Phys. Rev. D* **24**, 2848 (1981).
- [52] S. I. Nagorny, Yu. A. Kasatkin, and I. K. Kirichenko, Photodisintegration of the deuteron at $E_\gamma > 1$ GeV in the model of asymptotic amplitudes, *Sov. J. Nucl. Phys.* **55**, 189 (1992) [*Yad. Fiz.* **55**, 345 (1992)].
- [53] D. Binosi, J. Collins, C. Kaufhold, and L. Theussl, JaxoDraw: A Graphical user interface for drawing Feynman diagrams, version 2.0 release notes, *Comput. Phys. Commun.* **180**, 1709 (2009); D. Binosi and L. Theussl, JaxoDraw: A Graphical user interface for drawing Feynman diagrams, *ibid.* **161**, 76 (2004).
- [54] R. Mayer *et al.*, Beam-target double-spin asymmetry in quasielastic electron scattering off the deuteron with CLAS, *Phys. Rev. C* **95**, 024005 (2017).